Development of automated tip preparation for atom probe tomography by using script-controlled FIB-SEM

Jun Uzuhashi*, Tadakatsu Ohkubo and Kazuhiro Hono
National Institute for Materials Science, Tsukuba, 305-0047, Japan
**Corresponding author. E-mail: UZUHASHI.Jun@nims.go.jp*

Keywords: APT; atom probe tomography, FIB; focused ion beam, SEM: scanning electron microscopy, automation, scripting language

Abstract

Atom probe tomography (APT) has become a popular technique for microstructural analysis of a wide range of alloys and devices over the past two decades owing to the employment of laser-assisted field evaporation and the development of site-specific tip preparation using a focused ion beam (FIB) with a scanning electron microscopy (SEM) system. In laser-assisted field evaporation, laser irradiation conditions largely influence mass resolution; therefore, recent commercial APT instruments allow strict control of the analysis conditions. However, the mass resolution is affected not only by the laser condition but also by the thermal conductivity of the material and the tip shape. In addition, it is also important to keep the tip shape constant in order to obtain tomography data with good reproducibility since the analytical volume highly depends on the tip shape. In this study, we have developed a method to fabricate the tip with the desired shape automatically by using a script-controlled FIB-SEM system, which has traditionally depended on the skill of the FIB-SEM operator. The tip shape was then intentionally changed by using this method, and its effect on the APT data is also discussed.

Introduction

Atom probe tomography (APT) is the only technique that can visualize the three-dimensional distribution of atoms in materials [1-4]. In APT analysis, laser pulses or voltage pulses are applied onto the needle-shaped specimen (tip) under a high electric field to ionize atoms from the tip surface while simultaneously measuring the mass and position of those ions by a position-sensitive detector. Although the volume size that can be analyzed is limited to the nanoscale, the technique has a high spatial resolution close to atomic resolution and high chemical sensitivity with quantitative analytical capability. Two major technological innovations in the past 20 years have contributed to the APT technique becoming a powerful tool for microstructural analysis; one is the development of a laser-assisted atom probe [5-13] and the other is the establishment of a tip preparation method using a focused ion beam (FIB) with a scanning electron microscopy (SEM) system [14-18], which has broadened the APT applications to insulators, semiconductors, and their devices [19-23]. Furthermore, laser-assisted field evaporation, which uses laser pulses instead of voltage pulses, has dramatically reduced the frequency of tip fracture during APT measurement, which has been a traditional problem in the APT analysis [2, 5, 7]. The laser-assisted field evaporation resulted in a

significant improvement in the analysis yield and measurable volume size. It has also been reported that the use of femtosecond laser pulses, instead of nanosecond voltage pulses, greatly improves the mass resolution [2, 5]. On the other hand, laser-assisted evaporation often causes a mass tail issue in mass spectra, which degrades mass resolution [8-13]. The mass tail was reported to depend on several factors, including the laser irradiation conditions [7, 8, 10, 12, 24], the thermal conductivity of the material, and tip shape [9, 10, 25]. The latest commercial instruments, *i.e.,* CAMECA LEAP instruments, allow very precise control of measurement conditions such as laser power, wavelength, beam position, and evaporation rate. On the other hand, the tip fabrication for APT analysis still strongly depends on the skill and experience of the FIB-SEM operator. Since it is known that the tip shape strongly affects the mass resolution in the laser mode [2, 9, 10, 25], establishing a method to prepare tips reproducibly should make an important role to improve the reproducibility and reliability of APT data. In recent years, FIB-SEM systems can be automatically controlled by a scripting language, and an automated (or semi-automated) method of preparing samples for scanning transmission electron microscopy (S/TEM) has already been reported [26, 27]. In this study, we developed a method to fabricate tips in a specified shape automatically with high accuracy and reproducibility using a script-controlled FIB-SEM system. Automatically fabricated tips with intentionally different shapes were analyzed to study the effect of tip shape on APT data, and the underlying mechanism is also discussed in this paper.

Methods and Materials

A FIB-SEM system, Thermo Fisher Scientific Helios 5UX, was used to prepare APT tips. The instrument is equipped with an "AutoScript 4" system that can control the FIB-SEM system with a Python-based scripting language [28]. Python 3.6-based scripting allows control of various FIB and SEM conditions, image acquisition, processing fabrications, stage movement, etc., without any operator interactions. In addition to the standard Python library [29], the following open-source Python libraries were used in our scripting; ConfigObj 5.0.6 for reading and writing of configuration files [30], NumPy 1.15.4 for the mathematical algorithms [31], tifffile 2020.9.3 for reading image and metadata [32], Pillow 5.2.0 for opening and saving images [33], scipy 1.2.1 [34] and openCV 4.0.1 for image processing [35]. Since the purpose of this study is to control the tip shape, the lift-out process was performed manually [16, 18]. Note that the semi-automatic lift-out method has already been demonstrated by Tsurusawa *et al.* for S/TEM sample preparation [27], and fully automated lift-out is another challenge.

APT analyses were carried out for the automatically fabricated tips in the laser mode to compare how the APT data differs depending on the tip shape. CAMECA LEAP 5000XS was used for APT analysis with a 355 nm wavelength picosecond laser pulsing mode at a repetition rate of 500 kHz with the laser pulse energy 100pJ at a specimen base temperature of 50 K. The detection rate was kept constant at 2.0 %, that is, one ion per 50 laser pulses. It should be noted that all the tips were mounted on silicon support with platinum FIB deposition, and the sample height, the distance from the tip apex to the Si support was

approximately 3.0 μm. The obtained APT data were analyzed by CAMECA AP Suite Software 6.1.

Three alloys were used in this experiment: $Fe_{84.8}B_{10.9}P_{3.5}Cu_{0.8}$ nanocrystalline soft magnetic material, Cu-2.5Ni-0.8Si (mass%) Corson alloy, and commercial SUS304 stainless steel. The Fe-based nanocrystalline soft magnetic material is a promising candidate as a potential substitute for electrical steel sheets to improve the iron loss of electric motors at high frequency ranges for automotive applications [36, 37]. The Corson alloy is used in most electric appliances due to its excellent electrical conductivity and strength; thus, the alloy is one of the key materials to realize an energy-efficient society [38]. Since the properties of these alloys highly depend on the nanoscale three-dimensional structure, APT is an ideal tool to understand the relationship between the properties and the microstructures. In addition, stainless steel contains several trace elements and is a suitable material for comparing differences in mass resolution and chemical sensitivity in APT analysis. Therefore, these three alloys were used as examples for the establishment of the automated APT tip fabrication method in this study.

Results and Discussions

Figure 1 shows a schematic workflow of the automated tip fabrication process using a script-controlled FIB-SEM system. Once a Python-based program is executed, the FIB fabrication and monitoring of the tip shape from the SEM image is repeated automatically, until the tip shape becomes a set shape. The automated S/TEM sample fabrication method demonstrated by Tsurusawa *et al.* only performs the predefined FIB process [27]. However, since the sputtering yield by FIB varies depending on the material and crystal orientation [39, 40], it is impossible to maintain the reproducibility of the tip shape without sequentially acquiring SEM images and feeding the instantaneous tip shape back to the FIB process. The uniqueness of this study is that the FIB process is executed with active feedback from the SEM imaging, and this process flow improves the accuracy of fabrication.

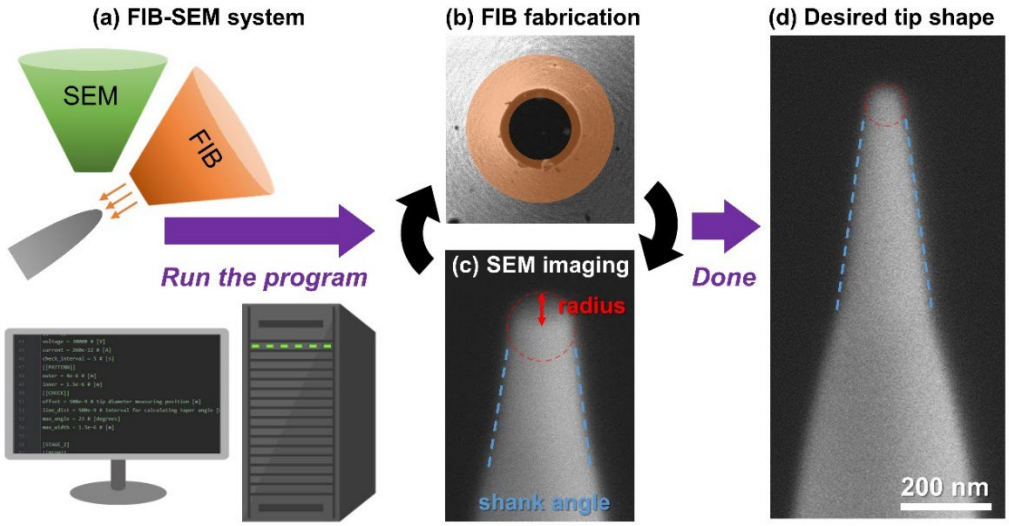

Figure 1. Schematic workflow of an automated APT tip preparation using a FIB-SEM system. (a) Execute the program on a script-controlled FIB-SEM system, (b) FIB fabrication

is carried out for a few seconds, and (c) the tip shape is monitored by using an SEM image. Repeating (b) and (c) until the tip becomes (d) the desired shape.

Figure 2(a) shows SEM images of the same silicon tip by an Everhart-Thornley detector (ETD), through-the-lens detector (TLD), and ion conversion and electron (ICE) detector (5kV, WD: 4mm) [41-43]. **Fig. 2(b)** shows the normalized intensity profiles from the arrows in **Fig. 2(a)**. The secondary electron images acquired with the out-lens type detectors (ETD and ICED) show left-right asymmetric contrasts. On the other hand, the intensity of secondary electron images acquired with through-the-lens detectors (TLD) is relatively symmetrical. The asymmetry of the intensity acquired with an out-lens type detector can be understood from the geometry of the detectors in the chamber as illustrated in **Fig. 2(c)**. Unlike judgment by the human eye, asymmetric contrast causes misrecognition by the boundary extraction program for monitoring the instantaneous change of the tip shape, so we have concluded that a through-the-lens SEM image is appropriate for monitoring the tip shape. A through-the-lens secondary electron image will henceforth be referred to as an "SEM image".

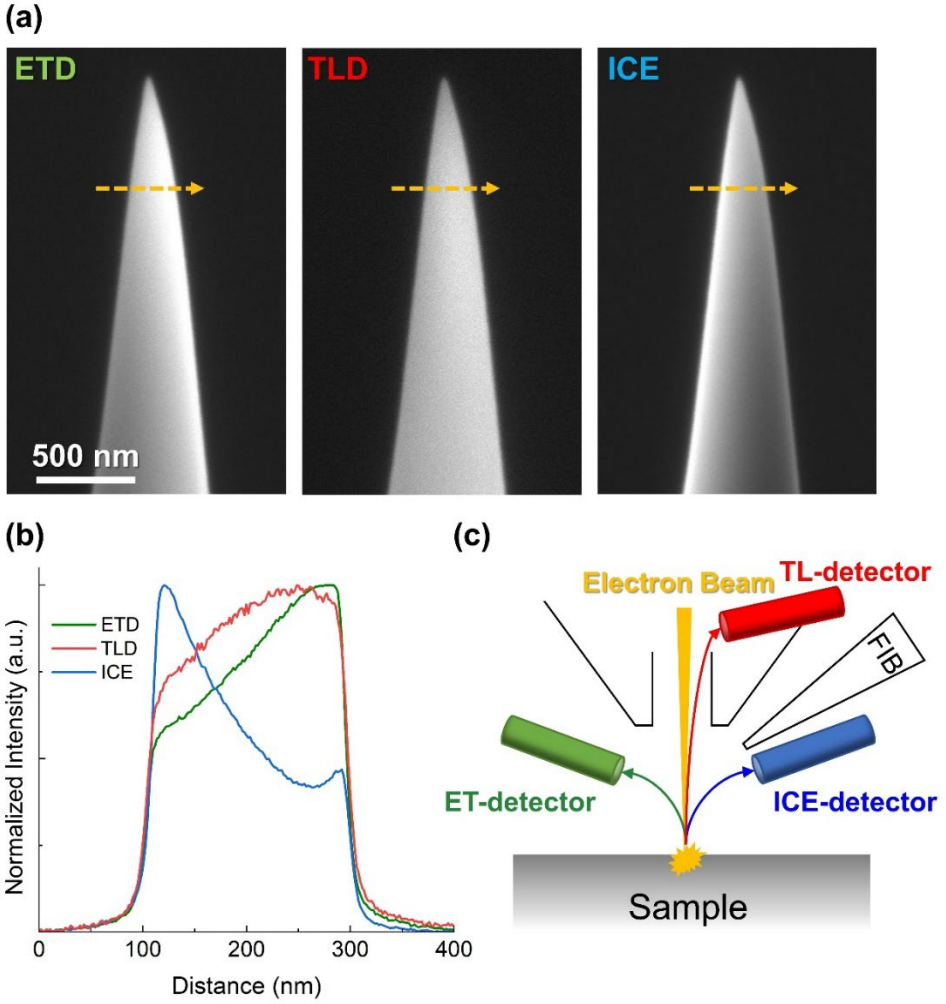

Figure 2. (a) Secondary electrons SEM images of the same silicon tip by using Everhart-Thornley detector (ETD), through-the-lens detector (TLD), and ion conversion and electron

(ICE) detectors. (b) Normalized SEM intensity line profiles from the arrows indicated in the SEM images. (c) Schematic of detectors geometry.

Figure 3(a) shows the definition of the tip shape and **Fig. 3(b)** shows an example of the tip observed by the SEM. A boundary extraction method called "canny edge detection" was applied to the SEM image for monitoring the tip shape [44]. Boundary extraction determines the position of the tip apex indicated by the yellow arrow in **Fig. 3(a)**. At the same time, the position where the width of the tip ("width: W_1" in **Fig. 3(a)**) is twice the radius of the tip curvature ("*r* (nm)" in **Fig. 3(a)**), *i.e.,* $W_1=2r$, is determined. In **Fig. 3(b)**, W_1 is 5.8×10^{-7} m, so the radius of this tip curvature is 1/2 of the value, *i.e.,* 290 nm. From the values of $W_{1\sim n}$ with constant interval "*d* (nm)" in the depth direction, the shank angle is calculated by linear approximation as illustrated in **Fig. 3(a)**. Based on the typical observing magnification when an operator performs APT tip preparation manually, "*d*" was set to 300~500 nm for rough fabrication and 200 nm for later FIB process. The "*n*", the number of measuring positions, was set as 5 in this study. The shank angle is 35.9° by linear approximation in the SEM image shown in **Fig. 3(b)**. In this way, the tip shape defined by the radius of the tip curvature and the shank angle can be monitored by the program.

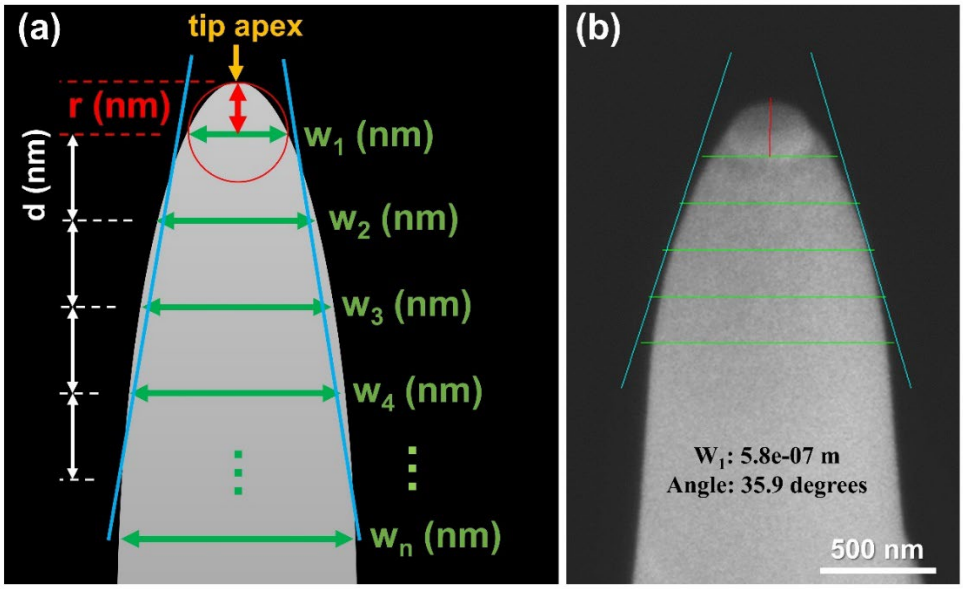

Figure 3. (a) Schematic of tip shape definition by the radius of the tip curvature and the shank angle. (b) Example of calculating the radius of the tip curvature and the shank angle by using the SEM image.

The next issue is the FIB fabrication conditions. In general, the APT tip fabrication is performed at 30 keV, followed by a cleaning process to remove Ga ion damage at 2~5 keV [2, 16]. Based on the typical FIB processes of manual APT tip preparation, three different fabrication conditions were set as shown in **Table 1**. The outer diameter of the donut-shaped sputtering mask was kept constant at 3~4 μm, and the inner diameter was gradually decreased according to the desired tip shape. The processing duration depends on the FIB sputtering

yield of the target material and the desired tip shape. In conventional operator-dependent processing, the operator must determine the size of the sputtering mask and processing duration based on his/her experience. In the automated fabrication method, on the other hand, if the tip shape does not meet the conditions specified in **Table 1**, the same process is repeated, and if the set conditions are satisfied, the next process is automatically started. During the process, SEM images are acquired every 5~10 seconds in the rough fabrication process, and every 2~3 seconds in the middle and later stages of the process. In addition, SEM images are acquired at a higher resolution than during rough milling so that monitoring the tip shape can be performed with high accuracy at the latter stages. This has made it possible to prepare the tip with high precision and reproducibility regardless of differences in sputtering yields of materials and crystal orientations. **Figure 4** shows automatically fabricated tips of nanocrystalline soft magnetic material using the three different conditions shown in **Table 1**. Shapes A and B have the same radius of tip curvature but different shank angles. Shape C has twice the radius of tip curvature as B. Although the images are not shown here, we were also able to fabricate tips with high precision in the case of the stainless steel and the Corson alloy. We analyzed these tips under the same APT measurement conditions to verify how the tip shape affects the APT data.

	FIB	Donut-shaped Mask (nm)				Parameters					
		Outer Diameter	A	B	C	Tip radius (nm)			Shank angle (degrees)		
			Inner Diameter			A	B	C	A	B	C
1	30 keV 0.26 nA	4000	1200			650			25	35	
2		3000	700			400			15	30	
3	30keV 90 pA	3000	300		400	200		250	13	25	
4		3000	170		200	60		125	10	25	
5	5 keV 21 pA	3000	0			50		100	10	25	

Table 1. Detailed fabrication steps and conditions for automated fabrications based on typical APT tips fabrication process. “Shape A, B, and C” are written as just “A”, “B”, and “C” in the table.

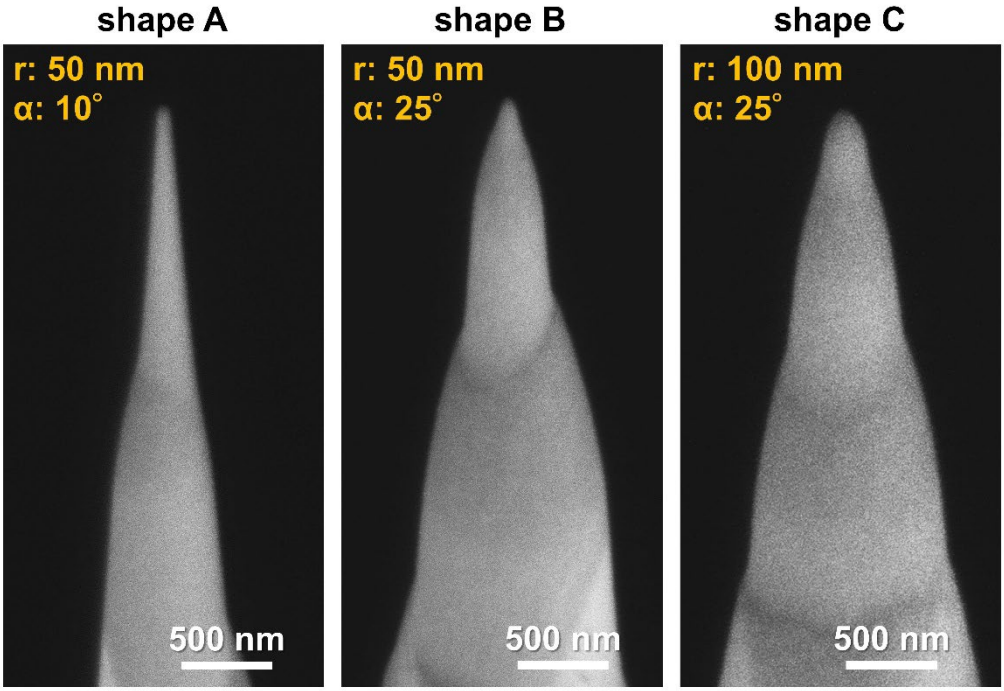

Figure 4. Automatically prepared APT tips from Fe-based nanocrystalline soft magnetic material with different conditions.

Figure 5 shows (a) a bright-field TEM image of the nanocrystalline soft magnetic material, (b) 2-nm-sliced elemental maps from the first 10 million atoms, and (c) mass spectra. As described in the previous report, the alloy has an amorphous phase surrounding bcc-Fe crystal grains of about 25 nm as shown in **Fig. 5(a)** [45]. In **Fig. 5(b)**, the Fe grains are visualized using an iso-concentrated surface with Fe=95 at%. Since the electric field on the tip surface is $F = \frac{V}{kr}$, where V is the applied DC voltage, k is a constant called the field factor and r is the tip radius, shapes A and B have the same field of view (FOV) immediately after the measurement starts, but the FOV of shape A hardly changes during measurement, while the FOV of shape B becomes larger. Shape C, on the other hand, has a radius of curvature twice that of A and B, so the FOV at the start of measurement is four times larger. The obtained 3D elemental maps reflect the shape of each tip. The difference in the mass spectrum shown in **Fig. 5(c)** is noteworthy. Comparing the mass resolution $m/\Delta m$ defined as the full width at half-maximum (FWHM), shape A is 185, B is 619, and C has 890. Shape A in particular shows a serious degradation in mass resolution; therefore, the $^{57}Fe^{++}$ and $^{58}Fe^{++}$ peaks are buried in the mass tail and barely discernible. This result is consistent with previous reports on the effect of tip shape on a mass resolution [9, 10]. That is, if the shank angle is small, the dissipation of the heat at the tip apex is reduced. Then, it leads to an increase in the unsynchronized evaporations with the laser pulses, resulting in an increase of the mass tail.

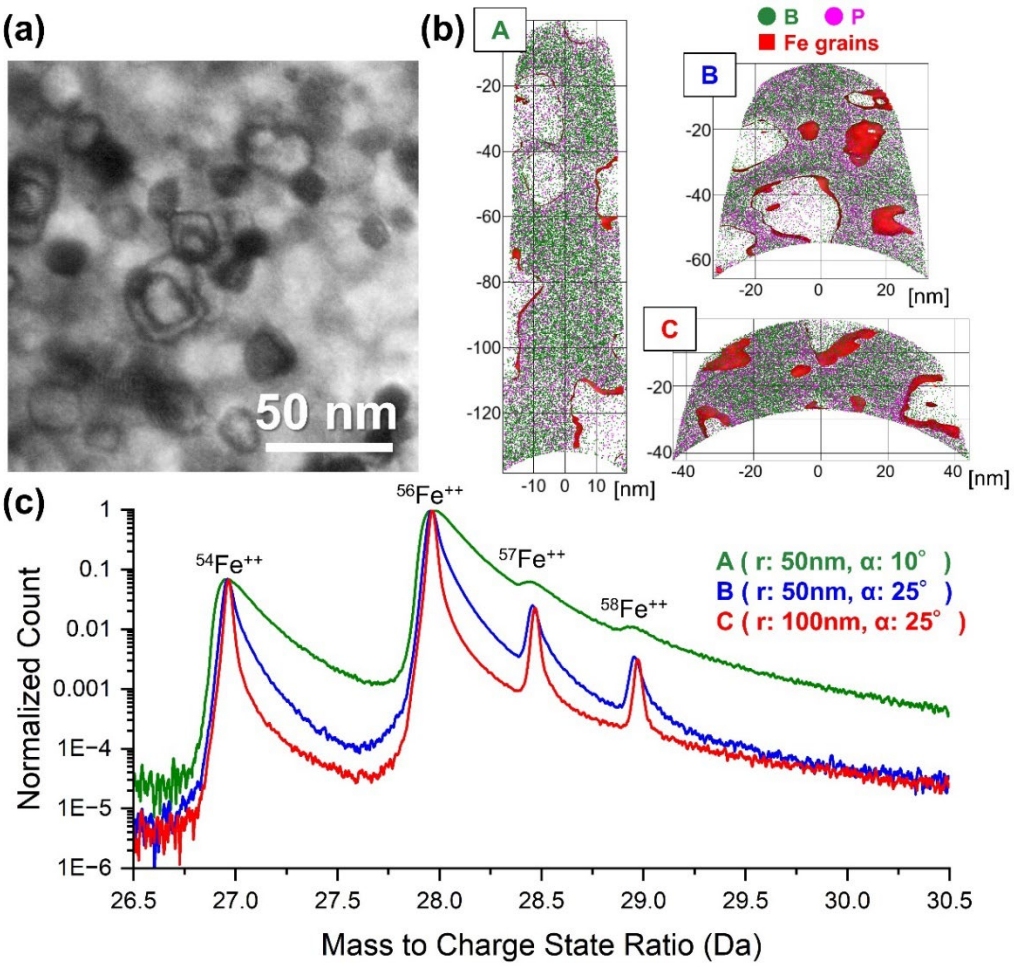

Figure 5. (a) Bright-field TEM image. (b) 2-nm-thick sliced 3D elemental maps reconstructed from the initial 10 million ions, and (c) mass spectra for Fe-B-P-Cu alloy. Iso-concentration surfaces at Fe of 95 at% are drawn to visualize Fe grains.

Figure 6 shows the APT mass spectra of (a) the stainless steel and (b) the Corson alloy. The $m/\Delta m$ value at FWHM of the stainless steel, which is a Fe-based alloy, is 191 for shape A, 534 for B, and 855 for C. The $m/\Delta m$ of **Fig. 6(a)** and **Fig. 5(c)** are in good agreement because both alloys are Fe-based materials. It is particularly noteworthy that the atom probe data of the stainless steel clearly shows differences in the detection sensitivity of trace elements, *i.e.,* $^{55}Mn^{++}$ and $^{59}Co^{++}$, due to differences in the magnitude of the mass tail. Copper alloys are a typical example known for frequent tip fractures during APT measurements in the voltage mode. We analyzed several tens of copper alloys in the voltage mode, but it was not possible to obtain APT data with a large volume due to frequent tip fractures. Thus, it can be adequately analyzed with a larger volume size in the laser mode. The mass resolution $m/\Delta m$ at FWHM of the Corson alloy shown in **Fig. 6(b)** was 476, 824, and 793 for shapes A, B, and C, respectively. The $m/\Delta m$ values for Fe-based nanocrystalline soft magnetic materials and stainless steels were in the order of C > B > A, whereas for Cu-based Corson alloy shows in the order of B~C > A (the difference between shape B and C is very slight). This difference may be due to the thermal conductivity of each alloy as discussed below.

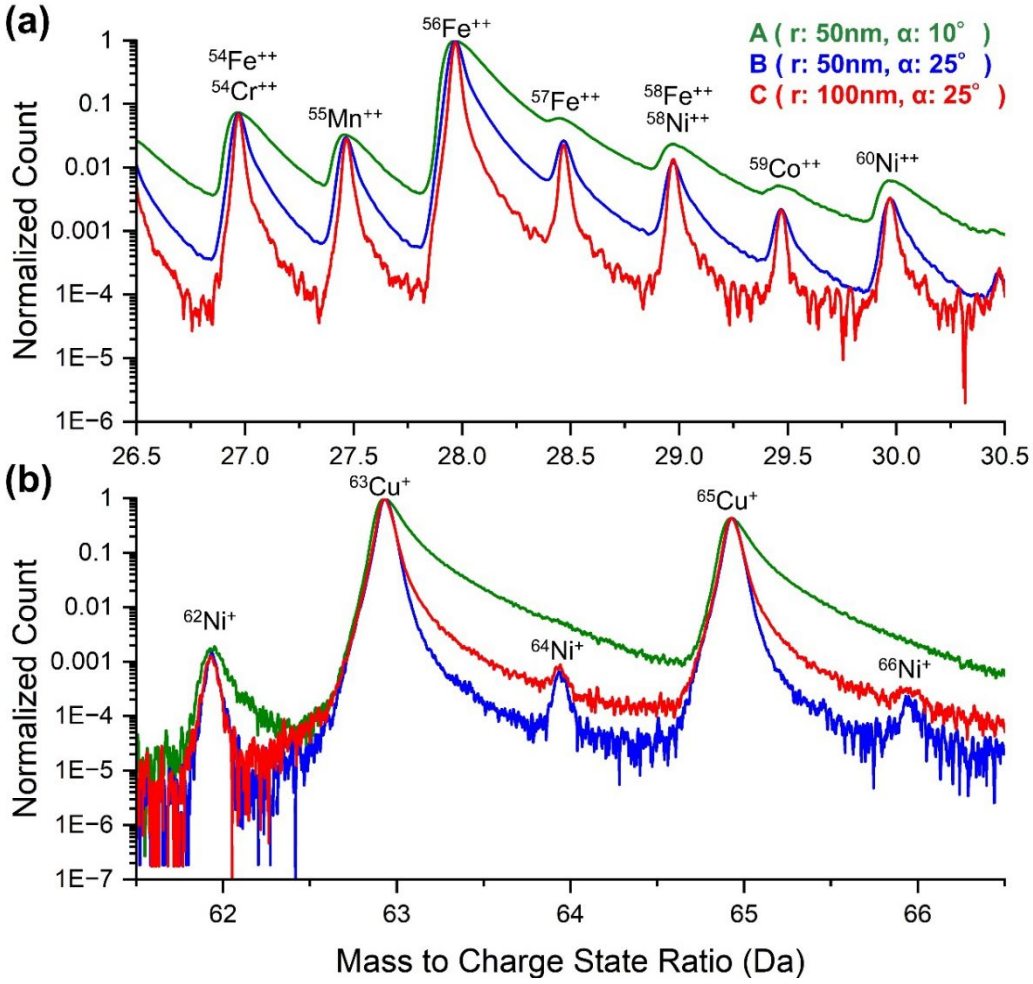

Figure 6. APT mass spectra for (a) stainless steel and (b) a Cu-Ni-Si Corson alloy.

The laser-assisted field evaporation is thought to be primarily triggered by the temperature rise due to laser irradiation, and if the temperature of the tip apex takes a longer time to cool down, the mass tail will appear and degrade mass resolution as a result [2, 8-10, 12, 13]. The quality of APT data depends not only on the tip shape but also on a complex combination of various factors such as the laser wavelength, beam spot size, pulse width, repetition rate, the materials absorption efficiency of the laser light, and so on [6-10, 12, 13], however, a simplified one-dimensional model is used here to discuss the effect of tip shape. According to previous studies [2, 46, 47], the APT tip can be considered as a stack of cylinders with different cross-sectional areas as schematically shown in **Fig. 7(a)**. Here, models with radii of tip curvature and shank angles corresponding to shapes A, B, and C were made for discussion. The laser spot size of LEAP5000XS is about 2.5 μm [48], thus, the Gaussian laser intensity profile along the tip can be drawn as **Fig. 7(b)**. The UV laser penetration depth is reported as 10 to 15 nm for Fe, Cu, and Si [49], thus, the absorbed energy is approximately proportional to the laser-illuminated area size (m^2). The laser-illuminated area along the tip direction can be calculated by considering the APT tip as a stack of cylinders. The Δz is set as 100 nm in this calculation, and z_0 indicates the tip apex. Therefore,

the absorption distribution of the laser along the tip was calculated as **Fig. 7(c)** by multiplication of the laser light intensity with the corresponding cylinder depth. By taking the cylinder volume size into account, the absorbed laser energy per unit volume was calculated in **Fig. 7(d).** The absorbed laser energy will be exchanged to the heat in each cylinder. In other words, the profiles shown in **Fig. 7(d)** indicate the initial temperature distributions by laser illumination in the tip shape A, B, and C. Due to a relatively larger volume size of tips with larger tip radius or shank angle, the order of temperature rises is C<B<A.

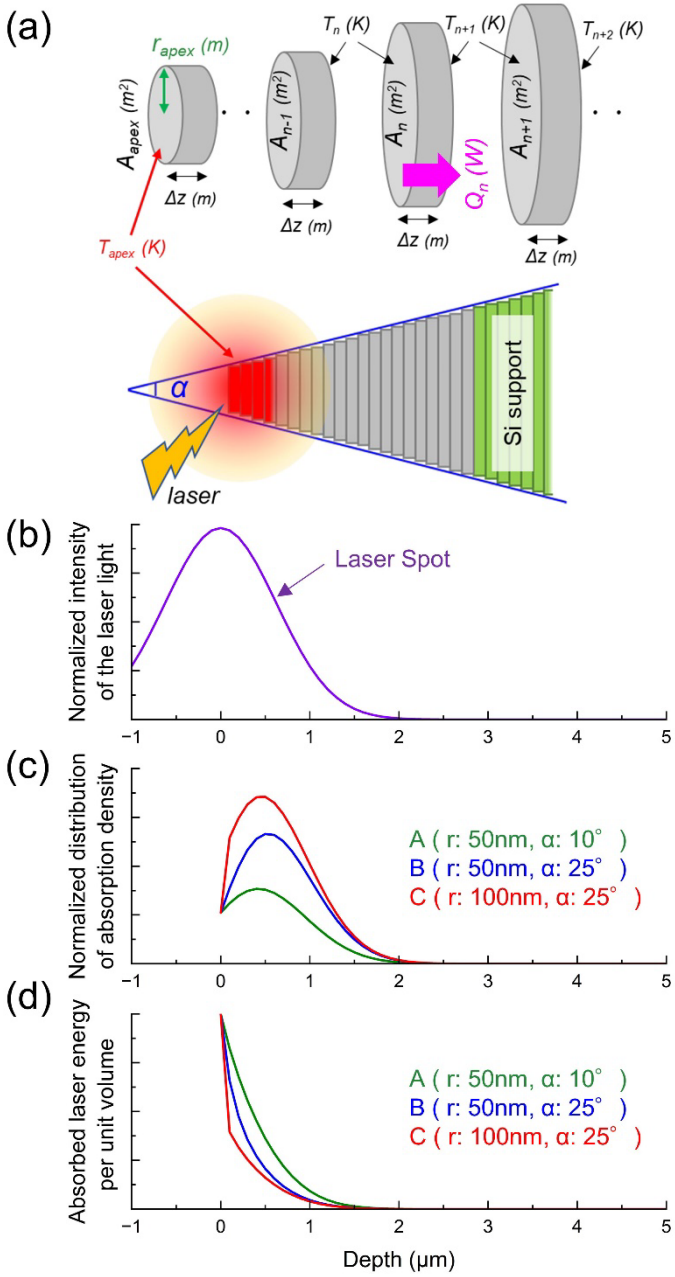

Figure 7. (a) Schematic illustration of a simplified model for the APT tip as a stack of cylinders with different cross-sectional areas. (b) The normalized intensity of illuminated laser with a spot size of 2.5 μm and (c) the absorption distribution of the laser along the tip. (d) The absorbed laser energy per unit volume.

When the laser irradiation is stopped, the tip immediately starts cooling down. The heat transfer in the APT tip should be complex, however, we treat the heat transfer problem by reducing it to a one-dimensional heat conduction equation to simplify the problem. That is, the heat generated by laser illumination is one-dimensionally transferred from the tip apex toward Si support through the cylinders with the different cross-sectional areas. The heat conduction equation is described as $\Delta T = \frac{Q}{\lambda A}$, where ΔT is the temperature gradient (K/m), Q is the amount of the heat (W), λ is the thermal conductivity of the material (W/mK), A is cross-sectional area (m^2) [50]. The temperature gradient at depth "z_n" ($z_n = n \times \Delta z$; $n=0, 1, 2, 3...$) is described as $T_n - T_{n+1} = \frac{\Delta z Q_n}{\lambda A}$. Since there is no heat generation without laser irradiation, the total amount of heat (W) is constant. Although the thermal conductivity of a material varies by temperature, the calculations here were performed using values at 50 K, which is generally set as the base temperature for APT measurements. The thermal conductivity of Cu is extremely high at 800 W/mK, while stainless steel is only 15 W/mK, and silicon used as support is 200 W/mK [50-54]. The thermal conductivities of a material are temperature dependent, but in this case, the order of values doesn't change in the range of 50 to 300 K [50-54]. Therefore, the calculations shown in **Fig. 8** were performed using constant thermal conductivities at 50 K. Note that the tip and Si support are bonded by Pt deposition; however, it was ignored in the calculations here. We assumed the temperature at 5 μm depth, far away from the tip apex, is well cold at 50 K in the model. Then, the one-dimensional temperature distributions after stopping the laser irradiation for stainless steel and Cu tips were calculated as **Fig. 8(a) and (b)**. A determination of the actual peak temperature is hard since it depends on too many factors [55, 56]; hence, **Fig. 8(a) and (b)** show the normalized temperature distributions along the tip after stopping laser irradiation. The thermal conductivity of Cu is so high that the heat should be dissipated faster from the tip apex; however, the calculated temperature distributions of the Cu tips (**Fig. 8(b)**) show gentle ones compared to the stainless steel (**Fig. 8(a)**). This tendency is due to the Si support having a much lower thermal conductivity (200 W/mK) than that of Cu (800 W/mK).

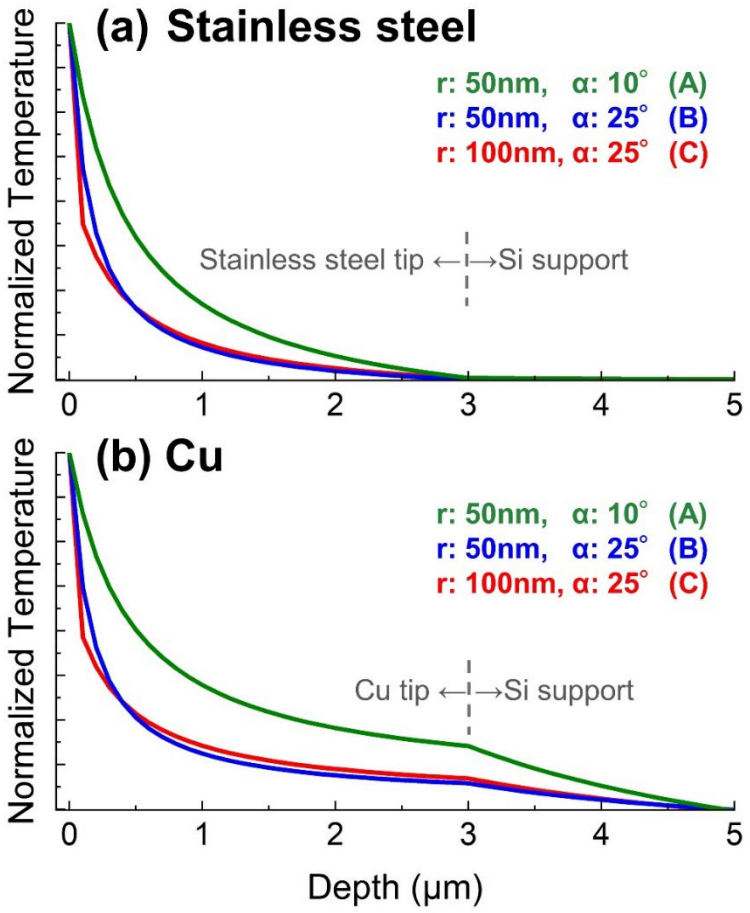

Figure 8. The normalized temperature distributions along the tip after stopping laser irradiation for (a) stainless steel tips and (b) Cu tips on Si support.

The unsteady-heat conduction is stated as:

$$\frac{\partial T}{\partial t} = \alpha \frac{\partial^2 T}{\partial z^2} \qquad (1)$$

, where α is the thermal diffusivity of the materials (m^2/s) according to previous studies on heat conduction problem [46, 50]. If "$T_{(n,\ i)}$" is defined as the temperature at depth "z_n" and at duration "t_i" ($t_i = i \times \Delta t;\ i=0, 1, 2, 3\ldots$), then, the following equation can be obtained by using a finite-difference method;

$$T_{(n,\ i+1)} = \Theta_z T_{(n+1,\ i)} + (1 - 2\Theta_z) T_{(n,\ i)} + \Theta_z T_{(n-1,\ i)} \qquad (2)$$

, where Θ_z is $\alpha \frac{\Delta t}{(\Delta z)^2}$ [57, 58]. The Eq. (2) is called *Forward Time Centered Space (FTCS)* approximation and detailed method can be found at [57, 58]. As the boundary condition, Eq. (2) can be applied if $0 < z_n < 5$ μm. For the z_n=0, Eq. (2) is described as:

$$T_{(0,\ i+1)} = 2\Theta_z T_{(1,\ i)} + (1 - 2\Theta_z) T_{(0,\ i)} \qquad (3)$$

The temperature is always kept at 50 K for z_n=5 μm (n=50). The thermal diffusivities of stainless steel, Cu, and Si are about $1\sim2 \times 10^{-3}$, $1\sim2 \times 10^{-5}$, and $1\sim2 \times 10^{-4}$ (m^2/s) at 50 K, respectively [54]. The thermal diffusivities are also temperature dependent, the values keep in

order of Cu＞Si＞stainless steel in a temperature range of 50 to 300 K. The temperature changes of the tip apex as the function of time were calculated in **Fig. 9(a) and (b)** for initial 20 ns by using the Eq. (2) and (3). As mentioned earlier, the cooling rate of the tip apex is considered to determine the magnitude of the mass tail [2, 8-10, 12, 13, 46, 47, 55, 56]. In the case of stainless steel, the temperatures are in the order of C<B<A, whereas the temperatures in the case of Cu are in the order of B<C<A (B is very slightly lower than C). However, the difference in this model calculation is much smaller than the experimental APT results. Although several unconsidered parameters should influence the cooling rate complicatedly, the calculation was carried out using a simplified one-dimensional model in this study; hence, the temperature changes in **Fig. 9** indicate the qualitative tendency. The model for close-to-reality calculation is required, however, it would be another challenge. Here, the tendency of calculated cooling rates of the tip apex is in good agreement with the APT mass tails shown in **Figs. 5(c) and 6**. Therefore, the calculations indicate that the thermal conductivity of the material and the tip shape affect the cooling rate of the tip apex after laser irradiation, which in turn affects the APT mass resolution.

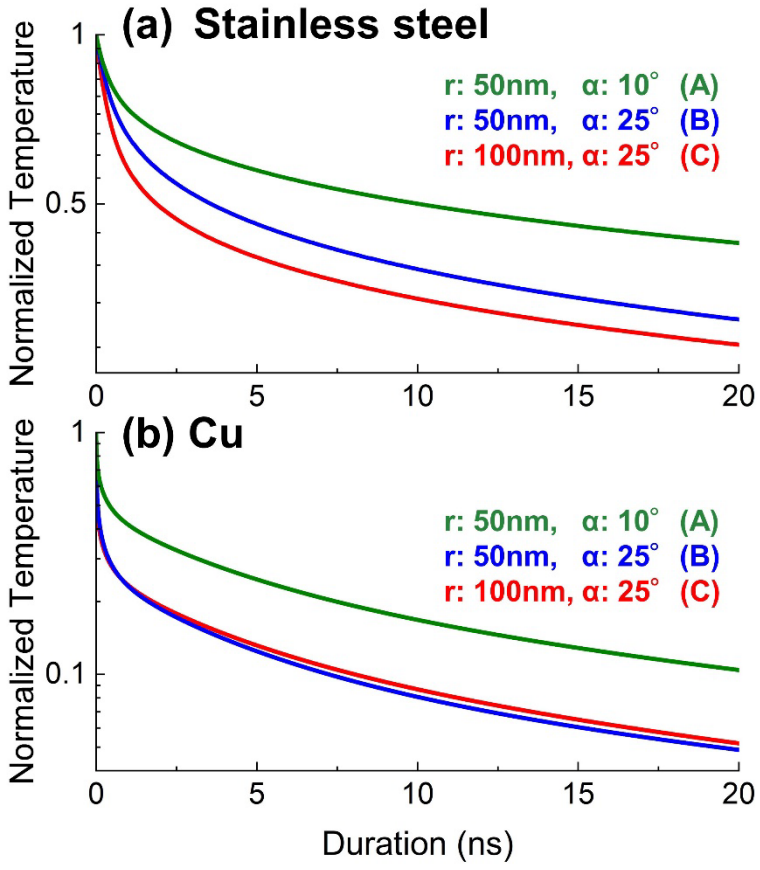

Figure 9. Calculated temperature changes of the tip apex as a function of the time for (a) stainless steel tips and (b) Cu tips on Si support.

As shown in the results above, the APT mass resolution in the laser mode differs even on the same alloy under the same measurement condition depending on tip shape. Hence, the

tip shape must be optimized according to the purpose of the APT analysis, so that the data quality can be kept the same. For example, if one wants to quantitatively compare microstructural differences in a series of the same alloy with different heat treatment conditions, it is important to maintain the same APT data quality. For this purpose, it is indispensable to have a method to fabricate tips with the same shape to improve the quantitative performance and reliability of APT data.

Conclusion

In summary, we have established a method to prepare APT tips with a specified shape by using a script-controllable FIB-SEM system. Using this method, tips with three different shapes were fabricated from a nanocrystalline soft magnetic material, stainless steel, and Corson alloy, and their APT results were compared. In the laser mode, there is a clear difference in the mass resolution depending on the tip shape even with the same alloy under the same measurement condition. The mechanism behind the difference in the APT data can be explained by the thermal conductivities of the materials and the tip shape using a simplified heat conduction model. Both experimental and calculation results strongly indicate that the automated tip fabrication method has a significant role to improve the reproducibility and reliability of the APT technique.

Acknowledgments

The authors thank Smart Solutions Inc. for supporting the writing of the scripting for the FIB-SEM dual beam system, Tohoku Magnet Institute Inc. for providing us with Fe-based nanocrystalline soft magnetic material, and Furukawa Electric Inc. for providing Corson alloy, and Kyoko Suzuki for technical support.

References

1. M.K. Miller, Atom Probe Tomography: Analysis at the Atomic Level, Kluwer Academic, New York, 2000. https://doi.org/10.1007/978-1-4615-4281-0
2. B. Gault, M. P. Moody, J.M. Cairney, S.P. Ringer, Atom Probe Microscopy, Springer Series in Materials Science, 2012. https://doi.org/10.1007/978-1-4614-3436-8
3. A. Cerezo, T.J. Godfrey, and G.D.W. Smith, Application of a position-sensitive detector to atom probe microanalysis, Rev. Sci. Instrum. **59**, 862 (1988). https://doi.org/10.1063/1.1139794
4. D. Blavette, B. Deconihout, A. Bostel, J.M. Sarrau, M. Bouet, and A. Menand, The tomographic atom probe: A quantitative three-dimensional nanoanalytical instrument on an atomic scale, Rev. Sci. Instrum. **64** (1993) 2911. https://doi.org/10.1063/1.1144382
5. B. Gault, F. Vurpillot, A. Vella, M. Gilbert, A. Menand, D. Blavette, and B. Deconihout, Design of a femtosecond laser assisted tomographic atom probe, Review of Scientific Instruments **77** (2006), 043705. https://doi.org/10.1063/1.2194089
6. A. Cerezo, G.D. Smith, Measurement of temperature rises in the femtosecond laser pulsed three-dimensional atom probe, Appl. Phys. Lett. **88** (2006), 154103. https://doi.org/10.1063/1.2191412

7. K. Hono, T. Ohkubo, Y.M. Chen, M. Kodzuka, K. Oh-ishi, H. Sepehri-Amin, F. Li, T. Kinno, S. Tomiya and Y. Kanitani, Broadening the applications of the atom probe technique by ultraviolet femtosecond laser, Ultramicroscopy **111**(2011), 576-583. https://doi.org/10.1016/j.ultramic.2010.11.020
8. J. Houard, A. Vella, F. Vurpillot, and B. Deconihout, Optical near-field absorption at a metal tip far from plasmonic resonance, Phys. Rev. B **81** (2010), 125411. http://dx.doi.org/10.1103/PhysRevB.81.125411
9. L. Arnoldi, A. Vella, J. Houard, and B. Deconihout, Antenna effect in laser assisted atom probe tomography: How the field emitter aspect ratio can enhance atomic scale imaging, Appl. Phys. Lett. **101** (2012), 153101. https://doi.org/10.1063/1.4757884
10. A. Cerezo, P.H. Clifton, A. Gomberg, G.D.W. Smith, Aspects of the performance of a femtosecond laser-pulsed 3-dimensional atom probe, Ultramicroscopy **107** (2007), 720-725. https://doi.org/10.1016/j.ultramic.2007.02.025
11. G. Sha, A. Cerezo, and G.D.W. Smith, Field evaporation behavior during irradiation with picosecond laser pulses, Appl. Phys. Lett. **92** (2008), 043503. https://doi.org/10.1063/1.2837626
12. J. Houard, A. Vella, F. Vurpillot, and B. Deconihout, Three-dimensional thermal response of a metal subwavelength tip under femtosecond laser illumination, Phys. Rev. B **84** (2011), 033405. http://dx.doi.org/10.1103/PhysRevB.84.033405
13. B. Mazumder, A. Vella, F. Vurpillot, G. Martel, and B. Deconihout, Surface carrier recombination of a silicon tip under high electric field, Appl. Phys. Lett. **97** (2010), 073104. https://doi.org/10.1063/1.3473816
14. D. J. Larson, D. T. Foord, A. K. Petford-Long, H. Liew, M. G. Blamire, A. Cerezo, G. D W Smith, Field-ion specimen preparation using focused ion-beam milling, Ultramicroscopy **79** (1999), 287. https://doi.org/10.1016/S0304-3991(99)00055-8
15. M. K. Miller, K. F. Russell, and G. B. Thompson, Strategies for fabricating atom probe specimens with a dual beam FIB, Ultramicroscopy **102** (2005), 287. https://doi.org/10.1016/j.ultramic.2004.10.011
16. K. Thompson, D. Lawrence, D. J. Larson, J. D. Olson, T. F. Kelly, and B. Gorman, In situ site-specific specimen preparation for atom probe tomography, Ultramicroscopy **107** (2007), 131. https://doi.org/10.1016/j.ultramic.2006.06.008
17. D. W. Saxey, J. M. Cairney, D. McGrouther, T. Honma, and S. P. Ringer, Atom probe specimen fabrication methods using a dual FIB/SEM, Ultramicroscopy **107** (2007), 756. https://doi.org/ 10.1016/j.ultramic.2007.02.024
18. M. K. Miller and K. F. Russell, Atom probe specimen preparation with a dual beam SEM/FIB miller, Ultramicroscopy **107** (2007), 761. https://doi.org/10.1016/j.ultramic.2007.02.023
19. A. K. Kambham, A. Kumar, A. Florakis, and W. Vandervorst, Three-dimensional doping and diffusion in nano scaled devices as studied by atom probe tomography, Nanotechnology **24** (2013), 275705. http://dx.doi.org/10.1088/0957-4484/24/27/275705
20. Cojocaru-Mirédin, O., Devaraj, A. & Guest Editors. Correlative microscopy and techniques with atom probe tomography: Opportunities in materials science. MRS Bulletin

47 (2022), 680-687. https://doi.org/10.1557/s43577-022-00369-4
21. Sasaki, T.T., Sepehri-Amin, H., Uzuhashi, J. et al. Complementary and correlative (S)TEM/APT analysis of functional and structural alloys. MRS Bulletin **47** (2022), 688-695. https://doi.org/10.1557/s43577-022-00374-7
22. McCarroll, I.E., Daly, L., White, L.F. et al. Atom probe tomography and correlative microscopy: Key techniques for future planetary science studies. MRS Bulletin **47** (2022), 696-705. https://doi.org/10.1557/s43577-022-00375-6
23. Rodenkirchen, C., Appleton, M., Ryan, M.P. et al. A review on atom probe and correlative microscopy studies of corrosion in nickel-based superalloys. MRS Bulletin **47** (2022), 706-717. https://doi.org/10.1557/s43577-022-00366-7
24. B. Gault, Y. M. Chen, M. P. Moody, T. Ohkubo, K. Hono, and S. P. Ringer, Influence of the wavelength on the spatial resolution of pulsed-laser atom probe, Journal of Applied Physics **110** (2011), 094901. https://doi.org/10.1063/1.3657846
25. M. Kodzuka, T. Ohkubo, K. Hono, Laser assisted atom probe analysis of thin film on insulating substrate, Ultramicroscopy **111** (2011), 557. https://doi.org/10.1016/j.ultramic.2010.11.008
26. B.V. Leer, R. Geurts, R. Scharfschwerdt, H. Cheng, L. Li, and R. Imlau, New Workflows Broaden Access to S/TEM Analysis and Increase Productivity, Microsc. Today **26** (2018), 18–25. https://doi.org/10.1017/S1551929517001195
27. H. Tsurusawa, N. Nakanishi, K. Kawano, Y. Chen, M. Dutka, B.V. Leer and T. Mizoguchi, Robotic fabrication of high-quality lamellae for aberration-corrected transmission electron microscopy, Scientific Reports **11** (2021), 21599. https://doi.org/10.1038/s41598-021-00595-x
28. R. Geurts and E.J.R. Vesseur, Novel SEM and DualBeam experiments with Python, Microscopy and Microanalysis **25** (2019), 236-237. https://doi.org/10.1017/S1431927619001910
29. https://python.readthedocs.io/en/stable/library/ (last accessed: Nov. 12, 2022)
30. https://configobj.readthedocs.io/ (last accessed: Nov. 12, 2022)
31. https://numpy.org/ (last accessed: Nov. 12, 2022)
32. https://doi.org/10.5281/zenodo.6795861 (last accessed: Nov. 12, 2022)
33. https://pillow.readthedocs.io/ (last accessed: Nov. 12, 2022)
34. https://scipy.org/ (last accessed: Nov. 12, 2022)
35. https://opencv.org/ (last accessed: Nov. 12, 2022)
36. Y. Yoshizawa, S. Oguma, and K. Yamauchi, New Fe-based soft magnetic alloys composed of ultrafine grain structure, Journal of Applied Physics **64** (1988), 6044. https://doi.org/10.1063/1.342149
37. A. Makino, H. Men, T. Kubota, K. Yubuta, A. Inoue, New excellent soft magnetic FeSiBPCu nanocrystallized alloys with high Bs of 1.9 T from nanohetero-amorphous phase, IEEE Trans. Magn. **45** (2009), 4302-4305. https://doi.org/10.1109/TMAG.2009.2023862
38. S. A. Lockyer & F. W. Noble, Precipitate structure in a Cu-Ni-Si alloy, Journal of Materials Science **29** (1994), 218–226. https://doi.org/10.1007/BF00356596
39. B. W. Kempshall and S. M. Schwarz, Ion channeling effects on the focused ion beam

milling of Cu, Journal of Vacuum Science & Technology B: Microelectronics and Nanometer Structures Processing, Measurement, and Phenomena **19** (2001), 749. https://doi.org/10.1116/1.1368670
40. G. Ran, S. Wu, X. Liu, J. Wu, N. Li, X. Zu, L. Wang, The effect of crystal orientation on the behavior of a polycrystalline tungsten surface under focused Ga+ ion bombardment, Nuclear Instruments and Methods in Physics Research Section B: Beam Interactions with Materials and Atoms **289** (2012), 39-42. https://doi.org/10.1016/j.nimb.2012.08.008
41. T.E. Everhart and R.F.M. Thornley, Wide-band detector for micro-microampere low-energy electron currents, J. Sci. Instrum. **37** (1960), 246. https://doi.org/10.1088/0950-7671/37/7/307
42. K. Kumagai, T. Sekiguchi, Sharing of secondary electrons by in-lens and out-lens detector in low-voltage scanning electron microscope equipped with immersion lens, Ultramicroscopy **109** (2009), 368-372. https://doi.org/10.1016/j.ultramic.2009.01.005
43. A.P. Conlan, E. Tillotson, A. Rakowski, D. Cooper, S.J. Haigh, Direct measurement of TEM lamella thickness in FIB-SEM, Journal of microscopy **279** (2019), 168-176. https://doi.org/10.1111/jmi.12852
44. M. Basu, Gaussian-based edge-detection methods-a survey, IEEE Transactions on Systems, Man, and Cybernetics, Part C (Applications and Reviews) **32** (2002), 252-260. https://doi.org/10.1109/TSMCC.2002.804448
45. Y. Nomura, J. Uzuhashi, T. Tomita, T. Takahashi, H. Kuwata, T. Abe, T. Ohkubo, K. Hono, Heating rate dependence of coercivity and microstructure of Fe-B-P-Cu nanocrystalline soft magnetic materials, J. Alloys Compd. **859** (2021), 157832. https://doi.org/10.1016/j.jallcom.2020.157832
46. H.F. Liu, and T. T. Tsong, Numerical calculation of the temperature evolution and profile of the field ion emitter in the pulsed-laser time-of-flight atom probe, Review of Scientific Instruments **55** (1984), 1779. https://doi.org/10.1063/1.1137658
47. H. F. Liu, H. M. Liu, and T. T. Tsong, Numerical calculation of the temperature distribution and evolution of the field-ion emitter under pulsed and continuous-wave laser irradiation, Journal of Applied Physics **59** (1986), 1334. https://doi.org/10.1063/1.336527
48. T.F. Kelly and K. Henry, Atom Probe Tomography of Semiconductor Nanostructures, Chapter 14 in "Metrology and Diagnostic Techniques for Nanoelectronics" (edited ByZhiyong Ma, David G. Seiler), Jenny Stanford Publishing (2016). https://doi.org/10.1201/9781315185385
49. Y. Tong, X. Liang, S. Bai and Q.H. Qin, Laser Ablation Applications in Ablation-Resistance Characterization of Materials, Book chapter 17 of "Applications of Laser Ablation" edited by D. Yang (2016). http://dx.doi.org/10.5772/65108
50. David W. Hahn, M. Necati Özisik, Heat conduction, Wiley (2012). http://dx.doi.org/10.1002/9781118411285
51. D.K. Ravikumar, Y. Than, W. Xu, and J. Longtin, Thermal considerations in the cryogenic regime for the BNL double ridge higher order mode waveguide, Phys. Rev. Accel. Beams **20** (2017), 093201. http://dx.doi.org/10.1103/PhysRevAccelBeams.20.093201
52. Glen A. Slack, Thermal Conductivity of Pure and Impure Silicon, Silicon Carbide, and

Diamond, Journal of Applied Physics **35** (1964), 3460. https://doi.org/10.1063/1.1713251
53. H. R. Shanks, P. D. Maycock, P. H. Sidles, and G. C. Danielson, Thermal Conductivity of Silicon from 300 to 1400°K, Phys. Rev. **130** (1963), 1743. https://doi.org/10.1103/PhysRev.130.1743
54. P. Duthil, Material Properties at Low Temperature, CAS - CERN Accelerator School: Superconductivity for Accelerators (2015), 77-95. https://doi.org/10.48550/arXiv.1501.07100
55. F. Vurpillot, B. Gault, A. Vella, M. Bouet, and B. Deconihout, Estimation of the cooling times for a metallic tip under laser illumination, Appl. Phys. Lett. **88** (2006), 094105. https://doi.org/10.1063/1.2181654
56. E.A. Marquis and B. Gault, Determination of the tip temperature in laser assisted atom-probe tomography using charge state distributions, Journal of Applied Physics **104** (2008), 084914. https://doi.org/10.1063/1.3006017
57. J.D. Hoffman, S. Frankel, "Numerical methods for engineers and scientists", CRC Press (2001). https://doi.org/10.1201/9781315274508
58. G.W. Recktenwald, Finite-difference approximations to the heat equation, Mechanical Engineering (2004). https://api.semanticscholar.org/CorpusID:14754846